PAPER

Check for updates

In situ synthesis of bimetallic selenides on green porous carbon: density functional theory-proven electrocatalysts for efficient water splitting

Anjana Sajeevan,[a] Nijash Neermunda,[a] Sampath Karingula,[a] Pooja,[b] Soumyajit Jana,[a] Ravindar Pawar [ID][b] and Yugender Goud Kotagiri [ID] *[a]

A dual synthetic engineering strategy is implemented to modify the electronic structure by integrating heterojunctions into a bimetallic selenide electrocatalyst employing a bead-like carbon skeleton framework within the catalyst. Here, we have synthesized a catalyst that is benign, porous, and graphitic, derived from the phytochemical extracts of the medicinal plant *Vitex negundo* Linn. Upon doping with a bimetallic selenide, it exhibits a conductive carbon layer on its surface. We also unveil a novel perspective on reducing metal ions using phytochemical extracts, wherein phytochemicals rich in long-chain polyphenols, flavonoids, lignans, terpenoids, and steroids function as both reducing agents and carbon scaffolds for the catalyst. Besides serving as a carbon support, it synergistically integrates cobalt and nickel selenides, enhancing catalytic activity while embedding metals within a graphene-like carbon matrix. The electrocatalyst exhibited notable performance in water splitting, achieving minimal overpotential and Tafel slopes for the HER and OER due to superior electrolyte diffusion characteristics attributed to its porous nature, also verified by density functional theory calculations as an enhancement in electronic structure modification and surface binding strength for reaction intermediates thereby playing a crucial role in improving electrocatalytic performance. These findings align with the mechanistic and experimental insights, further validating the significance of electronic structure modifications in enhancing catalytic efficiency for water splitting.

1. Introduction

The integral role of energy is increasing to ensure our quality of life. Hence, the use of energy resources is regarded as one of the most substantial challenges of contemporary society. Roughly 2 out of 10 people in the world still lack access to electricity.[1] To meet the increasing energy demands, the consumption of fossil fuels is rising, significantly contributing to social development, but also resulting in severe environmental pollution, particularly the excessive accumulation of carbon in the atmosphere, causing global warming.[2] Thus, the generation of energy with zero carbon emissions, addressing both energy demand and environmental issues, is a vital need and a potential hot cake in the real world.[3] Renewable energy sources hold a distinct advantage as a solution due to their capacity to generate energy repeatedly without producing greenhouse gas emissions, which is the proper balance of energy and environment,[4] but most of

these sources are irregular across regional, seasonal, and routine, suffering from major variations in supply.[5,6] In this context, electrolyzers, particularly water electrolyzers, can significantly contribute to the development of a sustainable energy system, thanks to their ubiquity and high energy current density coupled with minimal or zero emissions of harmful byproducts.[7] Electrochemical water splitting is regarded as a clean and sustainable technique for generating high-purity hydrogen.[8] It has a huge significance since it facilitates the oxygen evolution reaction (OER) and hydrogen evolution reaction (HER), yielding O_2 and H_2 as sole products, especially due to its ability to produce green hydrogen with practically zero emissions,[9,10] but its practical use is constrained by the sluggish kinetics of its half-reactions, possessing large activation energy barriers. Electrocatalysts are employed to bypass these kinetic limits, but they are generally impractical for mass production due to their reliance on costly noble metals like ruthenium (Ru) and iridium (Ir) for the OER, and platinum (Pt) for the HER.[11] If constructed from more economical materials, they still necessitate considerable and expensive energy input, rendering total water splitting problematic and depleting their widespread application in the hydrogen economy.

[a] *Department of Chemistry, Indian Institute of Technology Palakkad, Palakkad, Kerala 678 557, India. E-mail: yugenderkotagiri@iitpkd.ac.in*

[b] *Department of Chemistry, National Institute of Technology Warangal, Hanumakonda, 506004, India*

Significant efforts have been dedicated to the development of electrocatalysts with minimal or no precious metal composition. As a result, electrocatalysts have been extensively synthesized with carbon materials.[12] Carbon materials, including carbon nanotubes (CNTs), carbon nanofibres, and graphene, have variable structures, extensive surface area, robust controllability, and superior chemical and environmental stability along with distinctive ability to exist in several morphologies and exhibit highly adaptable electronic structures[13,14] making them the preferred candidates for atomic level design of catalysts.[15,16] Porous carbon compounds characterized by a high specific surface area and excellent stability have been extensively utilized as electrode materials for fuel cells, supercapacitors, and lithium-ion batteries.[17–19] These pores even boost HER/OER activity by serving as a substrate to facilitate hydrogen/hydroxyl adsorption, hence increasing the overall rate of electrocatalytic water splitting.[20] Also, graphitic carbon materials offer high electrical conductivity, enhanced crystalline structure, and distinctive physicochemical features, which promote ion diffusion and charge propagation.[21] Nonetheless, graphitic carbon materials like graphene possess drawbacks including elevated cost, intricate synthesis, and inadequate porous structure.[22]

There has been a constant push for novel synthetic routes for porous carbon due to its advantages, and indispensable applications in the field of energy. Their well defined nanostructures and tunable surface area were obtained from intricate chemical routes, employing highly corrosive and hazardous chemicals.[23] Several chemical methods were employed to fabricate nanostructured composites, particularly by the incorporation of integrated organic ligands and metal ions into the crystal lattice of metal–organic frameworks (MOFs), especially Zeolitic Imidazolium Frameworks (ZIFs), serving as self-sacrificial templates.[24,25] The systematic design of precisely aligned ZIF-derived carbon hybrid arrays with targeted morphology and composition helps many electrocatalytic applications. Xiao and coworkers reported the use of ZIF-67 to synthesize a bimetallic phosphide nanosheet for OER catalysis in an alkaline solution using an ion-assisted solvothermal approach.[26] Furthermore, they demonstrated a much enhanced capacity to avert structural or morphological damage during high-temperature pyrolysis, and they have substantial surface-to-volume ratios. Despite the characteristics of MOF-derived porous carbons, they exhibit several significant drawbacks, including low graphitization levels, poor diffusion efficiency, and a substantial electrochemically inactive surface area.[27]

The direct synthesis of carbonaceous compounds from biomass, given its renewable nature, high abundance, and low cost, promises a significant gain. The inherent ordered porosity structure of natural raw biomass can preserve its textural characteristics in the resultant carbon compounds, which are in great demand for different possible technological applications. This also offers an alternative pathway for the upcycling of various biomass feedstocks.[28] The OER and HER activities of carbon materials can be significantly enhanced by the introduction of heteroatoms (such as sulfur[29] and nitrogen[30]), transition

metals,[31] or transition metal chalcogenides,[32] nitrides,[33] and sulfides.[34] Transition metal-based materials possess unpaired d-orbital electrons, which are crucial in the electrocatalytic process. Nevertheless, the limited electrical conductivity and the tendency for aggregation hinder the attainment of peak performance and superior stability.[35] Consequently, the synthesis of hybrid-integration of transition metals with various functional nanomaterials to attain a synergistic catalytic effect represents a viable approach to improve water splitting efficiency and stability. Recent studies have concentrated on transition metal sulfides,[36] phosphides,[37] selenides,[38] and oxides[39] owing to their abundance, cost-effectiveness, and favorable electrical and optical characteristics. Rui Sun and coworkers recorded the *in situ* growth of Ni_3S_2 nanocrystals on nickel foam, exhibiting high HER activity attributed to the exposed (015) plane, which has a significant ability for water adsorption and dissociation in an alkaline electrolyte, leading to ideal free energy for H* adsorption.[40] Due to the electronic configuration of Se atoms, which is $4s^24p^4$, and being put within the same group as S atoms, transition metal selenides (*e.g.*, layered $MoSe_2$, WSe_2, and non-layered CoSe and NiSe) demonstrate analogous features to transition metal sulfides and possess remarkable electrocatalytic activity.[41] Also, due to the enhanced density and electrical conductivity of Se atoms, transition metal selenides (TMSes) have superior volumetric energy and rate capabilities compared to transition metal sulphides (TMSs).[42] Also, TMSes have more inherent electrical conductivity than TMSs and oxides due to the more metallic nature of the Se atoms.[43]

Thus, carbon nanomaterials integrated with transition metal selenides present a viable approach for the development of electrocatalysts for the overall water splitting reaction. Prior reports integrate $CoTe_{2x}Se_{2(1-x)}$ and $CoS_{2y}Se_{2(1-y)}$ with graphitized carbon-based composites demonstrating total water splitting.[44] Also, $(Ni,Co)Se_2$ nanocages attached on 3D graphene aerogel have been reported as a catalyst for water splitting. The elevated catalytic activity of $(Ni,Co)Se_2$ and the superior conductivity of the graphene sheets together augment water splitting efficiency.[45] All these procedures entail significant costs; however, eco-friendly methods address the primary issue of cost accessibility and ease of preparation. Also, the electrochemical performance of Ni/Co binary selenides significantly surpasses that of Ni and Co selenides individually. Wang *et al.* demonstrated that the bimetallic $Ni_{0.5}Co_{0.5}Se_2$ combines the advantages of both nickel and cobalt-based materials.[46]

The majority of literature on synthetic methods for carbon-supported nanoparticles employs reducing agents to convert metal salts into nanoparticles, necessitating an additional step to integrate carbon into the system, hence complicating the synthesis process. We present a new paradigm using phytochemical solution as a reducing agent for metal salts, wherein phytochemicals abundant in long chain polyphenols, flavonoids, lignans, terpenoids, steroids, and organic acids such as salicylic acid[47] serve as both active species and a carbon support for water splitting applications. Besides serving as a carbon support, it synergistically incorporates both cobalt and nickel selenides, significantly augmenting catalytic activity

while embedding metals within a graphene-like carbon matrix. This encapsulation exhibits significantly greater activity than conventional methods of carbon derived from polymers like PVP,[48] PVA,[49] and MOF-derived carbon like ZIF[27] having to spare high cost for the attractive morphological property and specific particle size, which the long chain polyphenols and other phytochemicals give in a "greener" way.

In this work, we have successfully synthesized a pseudo-core shell catalytic material that is environmentally benign, porous, soft-template assisted, graphitic, and heteroatom-doped from the phytochemical extracts of *Vitex negundo* Linn, a widely distributed medicinal plant found in subtropical regions. This green porous carbon (GPC) was doped with a bimetallic selenide, consisting of nickel and cobalt, having a blanket of conductive carbon on the surface. The synthesized electrocatalyst demonstrated commendable performance in water splitting processes, HER and OER catalysis, with the lowest overpotential of 366 and 578 at 10 mA cm^{-2} due to greater electrolyte diffusion properties compared to its precursors.

The green porous carbon (GPC) was doped with a bimetallic selenide consisting of nickel and cobalt, having a blanket of conductive carbon on the surface. The proportion of conductive carbon on the catalyst surface was optimized by modifying the amounts of plant extract used, and the resultant electrocatalyst was characterized through structural analysis techniques, including XRD, XPS and FT-IR, in addition to morphological and surface area analysis tools including FESEM, HRTEM, and BET. Subsequent to electrochemical characterizations, including practical water splitting applications employing a H cell, upon which the catalyst exhibited enhanced activity, the underlying mechanism of this activity was analyzed through DFT calculations, revealing a shift in the d band of the catalyst compared to its Fermi levels. This shift indicates an improvement in surface binding strength for reaction intermediates, which is pivotal in enhancing electrocatalytic performance, attributed to superior electrolyte diffusion properties compared to its precursors.

2. Experimental Section

2.1. Chemicals

Nickel nitrate hexahydrate (98.0%), cobalt nitrate hexahydrate (97.0%), potassium hydroxide pellets (85.0%) and selenium metal powder (99%) were purchased from SRL Chemicals. Isopropyl alcohol (99.0%), methanol and nitric acid were purchased from Nice Chemicals Pvt. Ltd. Nafion solution was purchased from Kanopy Techno Solutions, and commercial Pt/C (20 wt%) and RuO$_2$ (99.0%) were purchased from Sigma Aldrich. Methanol was bought from Genesys Chemicals Inc. All reagents were used without further purification. Water was supplied with an Elix-10 (Millipore, Germany) Water Purification System (15 MΩ cm^{-1}).

2.2. Characterization

Functional groups present on the catalyst were analysed using a Shimadzu IRTracer-100 FT-IR instrument and a Thermo Scientific FlashSmart Elemental Analyzer was used to quantify the amount of carbon and nitrogen in the samples. To figure out the reducing activity of the phytochemical extract, UV-visible absorption spectra of the samples were recorded using a Thermo Fischer Scientific (Evolution 201) UV-vis spectrophotometer. Raman measurements were run on a Horiba Labram HR Evolution system. X-ray powder diffraction (XRD) patterns in the Bragg's angle (2θ) range of 10 to 90° were collected at room temperature using a SmartLab X-Ray diffractometer from Rigaku Corporation with Cu K$_\alpha$ radiation (λ = 0.1541 nm). X-ray photoelectron spectroscopy (XPS) was carried out with a spectrophotometer, Omicron Nano Technology, UK, using Mg K$_\alpha$ (1253.6 eV) radiation from a double anode at 150 W. Binding energies for the high resolution spectra were calibrated by setting C 1s to 284.6 eV. The morphology was examined with a field-emission scanning electron microscope (FESEM, Carl Zeiss) and a high-resolution transmission electron microscope (HRTEM, JEOL JEM-2010) with the help of ImageJ software. N$_2$ adsorption analysis was conducted on an Autosorb IQ by Anton Par at 77 K using Barrett–Emmett–Teller (BET) calculations for the quantification of specific surface areas. Pore size distribution (PSD) was calculated *via* a density functional theory (DFT) method by using nitrogen adsorption data and assuming a slit pore model.[50] The hydrophilicity of the samples was analysed using a contact angle measuring system (Apex Instruments Pvt. Ltd).

2.3. Synthesis of green porous carbon (GPC)

GPC was made from *Vitex negundo* Linn (VN) leaves that were collected from the campus premises, which lies in the foothills of the western ghats region in Palakkad, Kerala, India, washed with DI water to remove dust, washed with distilled water, and dried at room temperature. In a typical synthetic procedure, dried leaves were pulverized into a fine powder, and 50 g of the thus obtained powder was added into a 1 L round bottom flask containing 450 mL of distilled water and 50 mL of methanol and stirred continuously for 12 h at 60 °C to yield VN extract, and subsequently maintained at room temperature, filtered through Whatman filter paper and used as a carbon source as well as a green reducing agent. The synthetic approach towards VN extract synthesis is detailed in the supporting information, Scheme S1. A fixed amount of GPC source was stirred continuously at 60 °C for 2 hours. The resultant liquid was maintained at 95 °C until the green chemical stabilized nanoparticles were produced by the complete evaporation of water. The resultant brown precipitate was collected, and ground using a mortar and pestle, and a fixed amount of the product mixture was placed in an alumina boat and subjected to pre-carbonization in a tube furnace at 240 °C for 2 hours in ambient air. The obtained material was subjected to carbonization for 2 hours at 800 °C in an inert atmosphere, and finally obtained GPC.

2.4. Synthesis of the GPC/NiCo nanocomposite

To a fixed amount of green chemical extract, equal weights of cobalt nitrate and nickel nitrate were added and heated at 60 °C

under continuous stirring, and the solution became brown indicating phyto-compound generation. The gel was held at 95 °C, until green chemical stabilized metal nanoparticles were formed, and was dried at 60 °C. The obtained material was subjected to precarbonization at 240 °C under ambient air followed by carbonization for 2 hours at 800 °C in an inert atmosphere, to obtain nickel cobalt nanoparticles covered by a GPC skeleton (GPC/NiCo).

2.5. Synthesis of GPC/Nickel cobalt selenides

GPC/NiCo nanoparticles and an excess of selenium powder were mixed in a 1:2 ratio and taken into an alumina boat and heated in a tube furnace at 220 °C for 2 hours in ambient air (precarbonization), and the obtained pre-carbonized composite was selenized at 800 °C in the same tube furnace, with a continuous flow of nitrogen gas to obtain a nickel cobalt selenide electrocatalyst (GPC/NiSe$_2$/CoSe$_2$). To optimize the amount of carbon in the final catalyst, the volume of green chemical extract taken initially was varied to 45 mL, 90 mL, 135 mL and 180 mL and GPC/Nickel cobalt selenides were synthesized, namely GPC/NiSe$_2$/CoSe$_2$-45, GPC/NiSe$_2$/CoSe$_2$-90, GPC/NiSe$_2$/CoSe$_2$-135 and GPC/NiSe$_2$/CoSe$_2$-180. The synthesis strategy employed is schematically represented in Fig. 1.

2.6. Electrochemical measurements

All electrochemical properties of the samples were measured with a conventional three-electrode system by a CHI 6054E electrochemical analyzer (Model 6054e, CH instrument, USA). The glassy carbon electrode (GCE) modified with various catalyst samples, a Hg/HgO (1.0 M NaOH) electrode and a graphite rod were used as the working electrode, reference electrode and counter electrode, respectively for HER studies and Pt was used as a counter electrode for OER studies. To prepare the ink, 3 mg of the sample was mixed with a 1 mL solution of Nafion, isopropyl alcohol, and water in a 1:12:12 ratio and sonicated for 2 hours. Two microliters of the dispersion were uniformly drop-cast over the surface of a glassy carbon electrode with a surface area of 0.071 cm^2, resulting in a catalyst loading of 0.0845 mg cm^{-2}, and the electrode was left to dry at room temperature overnight.

To assess the HER and OER activities of all the samples, linear sweep voltammetry (LSV) was performed in 0.1M KOH solution (pH $\sim$ 13) for acquiring the polarization curves and relevant Tafel plots. The reversible hydrogen electrode (RHE) and the formula $E_{RHE} = E_{Hg/HgO} + 0.14$ V + pH × 0.0591 V were used to calibrate all the potentials. Current densities are normalized by geometric electrode area (0.071 cm^2). All the electrochemical measurements were corrected against the ohmic potential drop using the equation, $E_{iR} = E_{RHE} - iR$

Here, E_{iR} is the iR corrected potential, E_{RHE} is the measured potential with respect to the RHE, i is the measured current of LSV, and R is the uncompensated resistance (R_s) as determined by collecting the AC impedance spectra (solution resistance) at open circuit potential.[51] All the acquired electrochemical data were repeated until the same outcome is obtained.

The resistance of the material was calculated from electrochemical impedance spectra (EIS) with frequencies ranging from 100 kHz to 0.01 Hz under the influence of an AC potential at open circuit potential.

2.7. Computational study details

Density functional theory (DFT) calculations were performed using the Vienna Ab initio Simulation Package (VASP).[52–54] The atomic percentage ratios in the supercell composition were determined through X-ray photoelectron spectroscopy analysis. Projector augmented wave (PAW) potentials, as formulated by
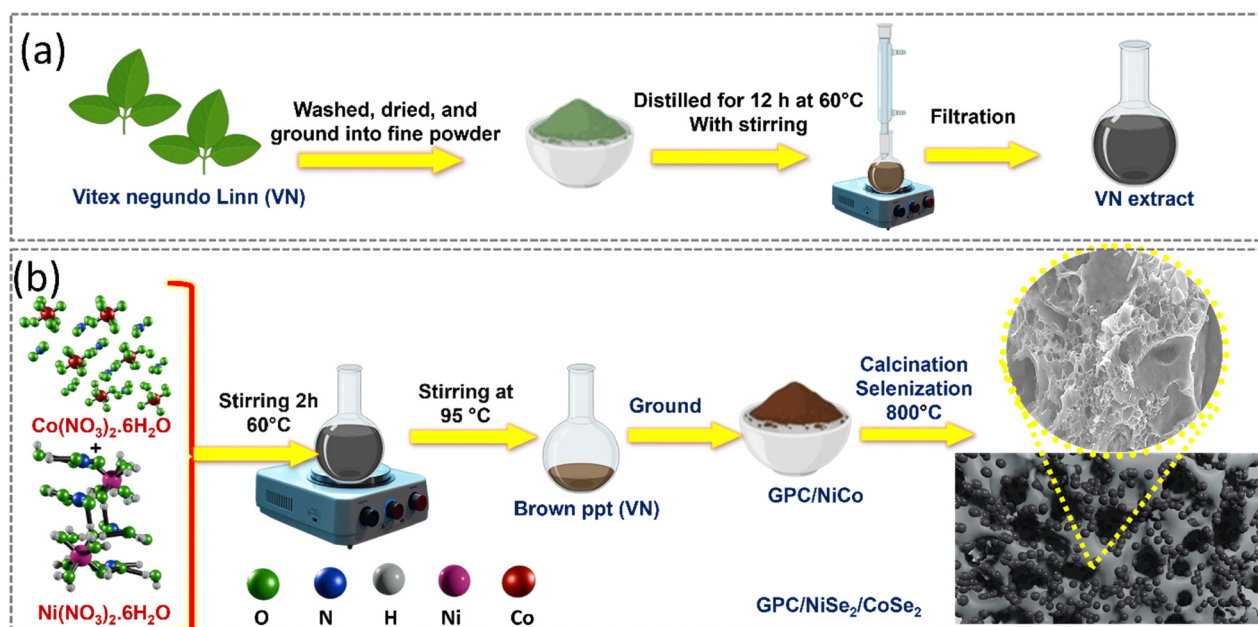

Fig. 1 Synthetic scheme adopted for the synthesis of the (a) GPC extract and (b) GPC/NiSe$_2$/CoSe$_2$ composite.

Kresse and Joubert, were employed to model the ion cores. The Perdew–Burke–Ernzerhof (PBE) generalized gradient approximation (GGA) was utilized to describe the electron exchange and correlation energies.[55–57] For all calculations, the PBEsol functional was implemented to enhance accuracy. Electron–core interactions were accounted for using PAW pseudopotentials obtained from VASP, with a plane-wave energy cutoff of 520 eV.[55–57] The valence states for the C $2s^2 2p^2$, Ni $3d^9 4s^1$, Co $3d^7 4s^2$, Se $4s^2 4p^4$, O $2s^2 2p^4$, and H $1s^1$ were considered. Geometry optimizations were performed until the energy variation was below 10^{-5} eV and the atomic forces were less than 0.01 eV Å^{-1}. The Brillouin zone was sampled using a Monkhorst–Pack Γ-centered grid of $2 \times 2 \times 1$.[58]

The differential charge density ($\Delta\rho$) was evaluated using the expression ($\rho(C_{\text{catalyst-intermediate}})-\rho(C_{\text{intermediate}})-\rho(C_{\text{catalyst}})$), where $\rho(C_{\text{catalyst-intermediate}})$ represents the electron density of the catalyst with the adsorbed intermediate, $\rho(C_{\text{intermediate}})$ denotes the electron density of the isolated intermediate species involved in the hydrogen evolution reaction and oxygen evolution reaction, and $\rho(C_{\text{catalyst}})$ corresponds to the electron density of the pristine catalyst. This methodology provides insights into charge redistribution during the reaction steps, elucidating the electronic interactions between the catalyst and the adsorbed intermediates. Cartesian coordinates of the structures are provided in the SI, Section S21.

3. Results and discussion

3.1. Structural characterization of the materials

UV-visible spectra were obtained to assess the reducing activity of the phytochemical-rich leaf extract. The spectra of the pure phytochemical, phytochemical–Co^{2+} complex solution, phytochemical–Ni^{2+} complex solution, nickel nitrate solution, and cobalt nitrate solution are presented in Fig. S1. A broad shoulder peak ranging from 305 nm to 370 nm, centered at 345 nm, was detected in the spectral data for the pure phytochemical solution, attributed to the π–π^* transition, while a peak at 514 nm was noted for the cobalt nitrate solution, resulting from the d–d transition. In the case of nickel nitrate solution, there is a pronounced absorption at approximately 396 nm, indicative of a d–d transition.[59] The d–d transition peaks at 514 nm and 396 nm in the phytochemical–Cobalt(II) and phytochemical–Nickel(II) mixture, respectively, vanished, and the broad shoulder peak was shifted. This implies the formation of cobalt and nickel nanoparticles by using the activity of phytochemicals for reduction.[60,61]

Fourier transform infrared spectroscopy (FT-IR) analysis was conducted for structural characterization and to examine the molecular interactions among various species and the elemental composition of the porous carbon supported bimetallic selenide composite and its precursors (Fig. 2a). The IR spectrum of all three samples (GPC, GPC/NiCo, and GPC/NiSe$_2$/CoSe$_2$) exhibits a broad IR band at 3440 and 2918 cm^{-1}, corresponding to –OH and C–H stretching vibrations, respectively. The bands at 1626 and 1380 cm^{-1}, consistently observed across all structures, signify the composite nature of the material, consisting of sp^2 C=C and sp^3 C–C carbon bonds.[62] The distinct sharp bands at 675 and 755 cm^{-1} were attributed to the metal selenide vibration, corroborating the formation of metal selenide.[63]

The presence of heterogeneous carbon structures and pores in the material is confirmed by Raman spectroscopy. Fig. 2b illustrates that the three composite materials exhibit distinctive
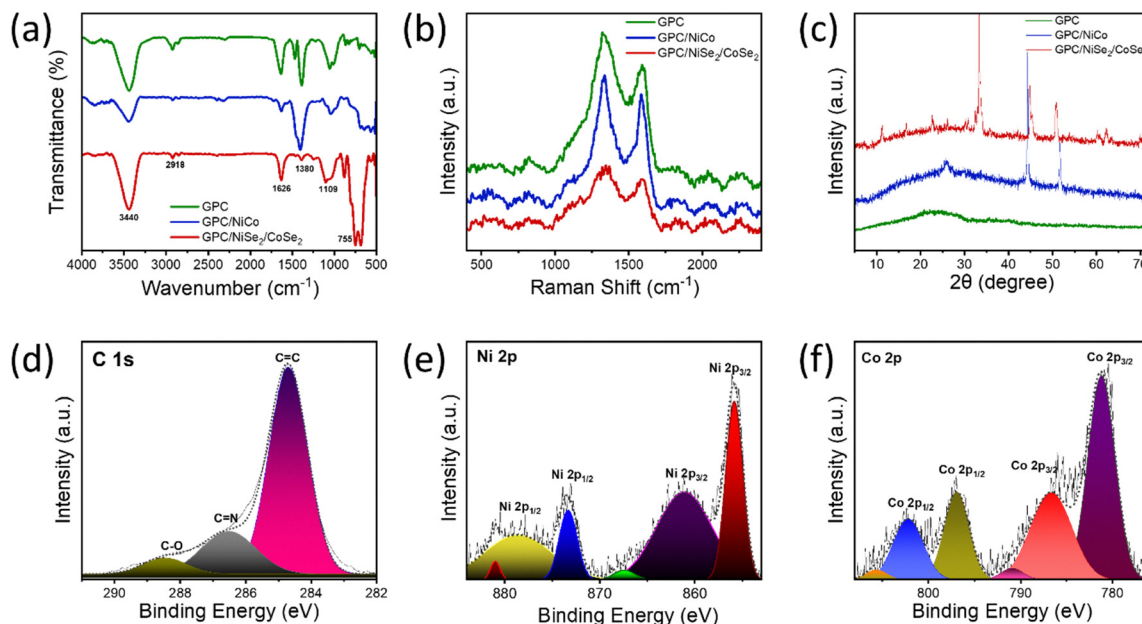

Fig. 2 (a) FT–IR bands, (b) Raman spectrum, (c) XRD patterns of GPC, GPC/NiCo and GPC/NiSe$_2$/CoSe$_2$ and deconvoluted XPS spectrum of (d) C 1s, (e) Ni 2p, and (f) Co 2p of GPC/NiSe$_2$/CoSe$_2$.

peaks at roughly 1335 and 1587 cm^{-1}, corresponding to the D (I_D) peak from disordered carbon and the G (I_G) peak from the in-plane stretching vibration of C=C atoms, respectively.[64] The D/G peak intensity ratio (I_D/I_G) is a critical metric for assessing the graphitization degree of the material, with values of 1.006851, 1.007713, and 1.014574 for GPC, GPC/NiCo, and GPC/NiSe$_2$/CoSe$_2$, respectively, indicating an increased generation of defects in the C=C network after selenium doping. The small displacement of the D band towards higher frequencies for GPC/NiSe$_2$/CoSe$_2$ results from the augmented structural disorder of the graphitic layer caused by the incorporation of selenium during the process.[65,66] The porosity created by the graphitic carbon layer is confirmed using Raman studies. Fig. 2c shows the XRD pattern of the as-prepared GPC/NiSe$_2$/CoSe$_2$, GPC/NiCo and GPC nanocomposite and the diffraction peaks can be ascribed to the combination of CoSe$_2$ (JCPDS No. 09-0234) and NiSe$_2$ (JCPDS No. 88-1711). The peaks from carbon are not detected in the final composite GPC/NiSe$_2$/CoSe$_2$ XRD pattern, due to the relatively low intensity of carbon compared to the GPC/NiCo and GPC. It is important to note that the carbon intensity in precursor GPC was also low; the region is magnified for enhanced visibility. Also, the CHNS elemental analysis confirmed the presence and growing proportion of carbon during the optimization phase, as illustrated in Fig. S2.

To explore the valence states of elements in the porous carbon-supported bimetallic selenides, X-ray photoelectron spectroscopy (XPS) spectra have been collected (Fig. 2d–f and Fig. S3, S4). The XPS survey scan spectrum of GPC/NiSe$_2$/CoSe$_2$ revealed the presence of C, Co, Ni, and Se components (Fig. S3). The C 1s XPS signal may be deconvoluted into three peaks located at 284.7, 286.59, and 288.53 eV (Fig. 2d), corresponding to C–C/C=C,[67] C=N, and C–O species, respectively,[68,69] signifying the existence of sp^{2}C graphitic layers doped with nitrogen. In the hydrogen evolution process, the nitrogen-doped graphitic carbon exhibits a partial negative charge, resulting in a robust adsorption capacity for hydrogen and an enhancement of HER catalytic activity. The co-doping of cobalt and nickel was validated by the deconvoluted XPS spectrum, which exhibited peaks corresponding to Ni^{2+}, Ni^{3+}, Co^{2+}, and Co^{3+}. The peaks at 855 eV and 873 eV correspond to Ni^{2+}, while the peaks at 861 eV and 878 eV indicate Ni^{3+} as shown in Fig. 2e.[66] In the Co 2p spectrum depicted in Fig. 2f, the two peaks at 781.2 eV and 796.7 eV correspond to the Co 2p$_{3/2}$ and Co 2p$_{1/2}$ orbitals, respectively, indicating the +2 valence state of the cobalt ion, while the peaks at 786.7 eV and 802.27 eV confirm the presence of Co^{3+}.[70] In addition to this, Fig. S4 shows the Se 3d spectrum, where the characteristic peaks at 55.4 eV and 54.3 eV correspond to the Se 3d$_{3/2}$ and Se 3d$_{5/2}$ orbitals, respectively, indicating the Co–Se and Ni–Se chemical bonds. Alongside the two characteristic peaks, an additional peak at 58.9 eV can be attributed to the SeO$_x$ component.[70,71] Ni and Co exhibit surface reconstruction, shuttling between two oxidation states, confirmed by XPS and through the partial exchange of their anions with oxide/hydroxide, leading to a structure which facilitates the OER and charge transfer, hence improving OER activity.[72]

3.2. Morphological characterization of the materials

The morphology and particle size of the synthesized porous carbon derivatives have been explored using SEM and TEM. The surface morphology of different catalysts at various magnifications is provided in Fig. 3. Fig. 3(a–c) illustrates that GPC exhibits a morphology that features stacked graphitic sheets in lower dimensions with unique pores. Upon the introduction of metals, carbon serves as a framework for the uniform distribution of metal nanoparticles, as illustrated in Fig. 3(d–f). The particles are distinctly separated, lacking any agglomeration These function as a highly dispersed nanoparticle catalyst, exhibiting enhanced electrochemical activity. Cobalt and nickel nanoparticles are embedded in a carbon support, augmenting the catalytic properties. Furthermore, porosity is more pronounced in the structure, enhancing the proximity of electrolytes to the active electrode. During the selenization of NiCo nanoparticles, porosity is preserved, as revealed in Fig. 3(g–i). The composite exhibited a sponge-like morphology, facilitating enhanced electrolyte penetration compared to prior catalysts. The spongy nature of the catalyst was retained post catalytic activity, as evident from Fig. S5.

The carbon skeleton is more apparent as a conductive layer, as illustrated in the TEM micrographs in Fig. 4a and b. Alongside spherical nickel and cobalt particles, tiny defects are evident in the graphite ribbons, indicating the presence of micropores.[73] The pores form due to the leaving groups situated between the carbon sheets, as established by the High Resolution TEM (HRTEM) images in Fig. 4c. These macro-pores facilitate the flow of electrolyte ions into the inner micro-pores. A conductive carbon blanket encases the metal selenides with a thickness of few nanometers as shown in Fig. 4d.[74] The modification of the carbon blanket was essential for improving electrocatalytic activity, as fewer carbon layers with numerous faults and edges increased the proximity of exposed active sites and aided the diffusion of electrolytes and H$_2$.[74] Utilizing FFT and IFFT, we computed d-spacing values that corresponded with those acquired from XRD (Fig. 4e). The SAED data also exhibited a strong correlation with the XRD peaks (Fig. 4f). Analyzing the HRTEM images in Fig. 4e indicated that the spacings of 0.287 nm and 0.24 nm correspond to the (111) plane of NiSe$_2$ and the (100) plane of CoSe$_2$, respectively. Also, Fig. 4e shows a spacing of 0.33 nm, attributed to the (002) plane of graphite-like carbon layers. Elemental mapping demonstrated the uniform distribution of Ni and Co throughout the designated detection range of the composite, in conjunction with carbon (Fig. 4h), and particle size distribution analysis confirmed that most of the particles lie in the diameter range 25–30 nm (Fig. 4g).

3.3. Surface area analysis

N$_2$ adsorption studies were conducted to assess the porosity of the samples. The histogram of Brunauer–Emmett–Teller (BET) surface area (Fig. 5a) reveals that GPC/NiSe$_2$/CoSe$_2$ possesses the largest BET area (87.626 m^2 g^{-1}), exceeding that of the precursors GPC/NiCo (82.377 m^2 g^{-1}) and GPC (22.454 m^2 g^{-1}).
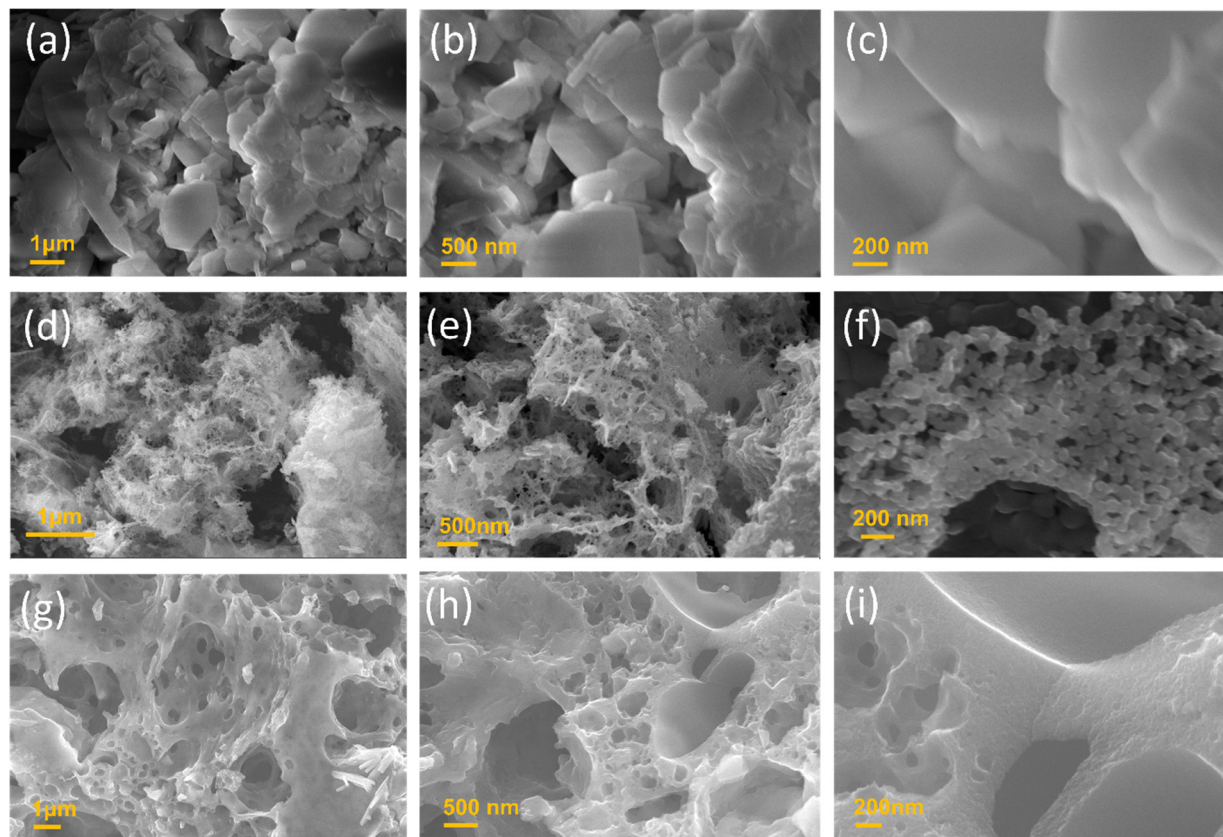
Fig. 3 FESEM morphology of GPC (a)–(c), NiCo nanoparticles supported on GPC (d)–(f), and NiSe$_2$/CoSe$_2$ supported on GPC (g)–(i).

To elucidate the significant disparities in the porous architectures of the precursor compounds, their pore size distribution curves have been studied and detailed in Fig. 5b and Fig. S6, S7. The pore size distribution graphs for GPC and GPC/NiCo exhibit only a small number of mesopores, leading to reduced BET surface areas. Alongside substantial mesopores, numerous tiny mesopores developed on the GPC/NiSe$_2$/CoSe$_2$ surfaces (Fig. 5b), resulting in an increased BET surface area of GPC/NiSe$_2$/CoSe$_2$ relative to GPC and GPC/NiCo. The results establish that all the GPC/NiSe$_2$/CoSe$_2$ material is highly nanoporous in nature with most of the pore surface area populated primely between $\leq$ 2 nm pore width. Among the two samples, GPC/NiSe$_2$/CoSe$_2$ possessed very high active surface area with pore widths specifically $\leq$ 2 nm to an extent of 80.85 m^2 g^{-1} ($\sim$92%) out of 87.81 m^2 g^{-1}. Compared to GPC/NiSe$_2$/CoSe$_2$, the active surface areas of GPC/NiCo with pore widths $\leq$ 2 nm were quite low and were 42.68 m^2 g^{-1} (53%), and nanopores of $\leq$ 2 nm pore width will be effective for percolation and free movement of ions and substrates at electrode–electrolyte interface. This structural property can boost the doping of bimetallic selenides into carbon structures by increasing the availability of active sites, hence promoting the catalytic activity for the HER and OER. The trend followed in BET surface area was further augmented by electrochemical active surface area (ECSA) analysis of the synthesized composite *via* calculating the geometric double layer capacitance (C_{dl}) within a potential range of 0 V to 0.2 V *vs.* Hg/HgO at scan rates between 100 and 6.25 mV s^{-1},[75] (Fig. S8) in 0.1M KOH solution and the resulting double layer capacitance is provided in Fig. 5c. The capacitance values are directly proportional to the ECSA, calculated by the formula ECSA = $C_{\text{dl}}/C_{\text{s}}$ (S9). Fig. 5d illustrates that the C_{dl}, and thus ECSA value of GPC/NiSe$_2$CoSe$_2$ is markedly superior to that of other materials, indicating an increased number of accessible active sites and varied pathways for charge transfer, ion exchange, and mass transfer, thereby leading to a substantial enhancement in catalytic performance. The double layer capacitances of GPC/NiSe$_2$/CoSe$_2$, GPC/NiCo, and GPC are 3.14, 2.15 and 0.219 mF cm^{-2}, respectively. In comparison to the double layer capacitance of bare green porous carbon, a tenfold rise is found in GPC/NiCo, with capacitance further escalating by 15 times upon selenization, as proven by the superior C_{dl} value of GPC/NiSe$_2$/CoSe$_2$ among all three materials. The samples containing GPC/NiSe$_2$/CoSe$_2$ have a significantly elevated ECSA compared to those of GPC/NiCo and GPC as evident from Table S9. This supports our design assumption that bimetallic selenide catalysts facilitate the etching of carbon and produce more pores. Consequently, a greater number of active sites are accessible to the electrolyte and engage in the catalysis. The comparison of ECSA and BET surface area was plotted in Fig. 5d and GPC/NiSe$_2$/CoSe$_2$ shows the highest surface area in both cases, indicating that a higher count of active sites is available for electrochemical reaction and thus enhancing electrocatalytic performance.[76]
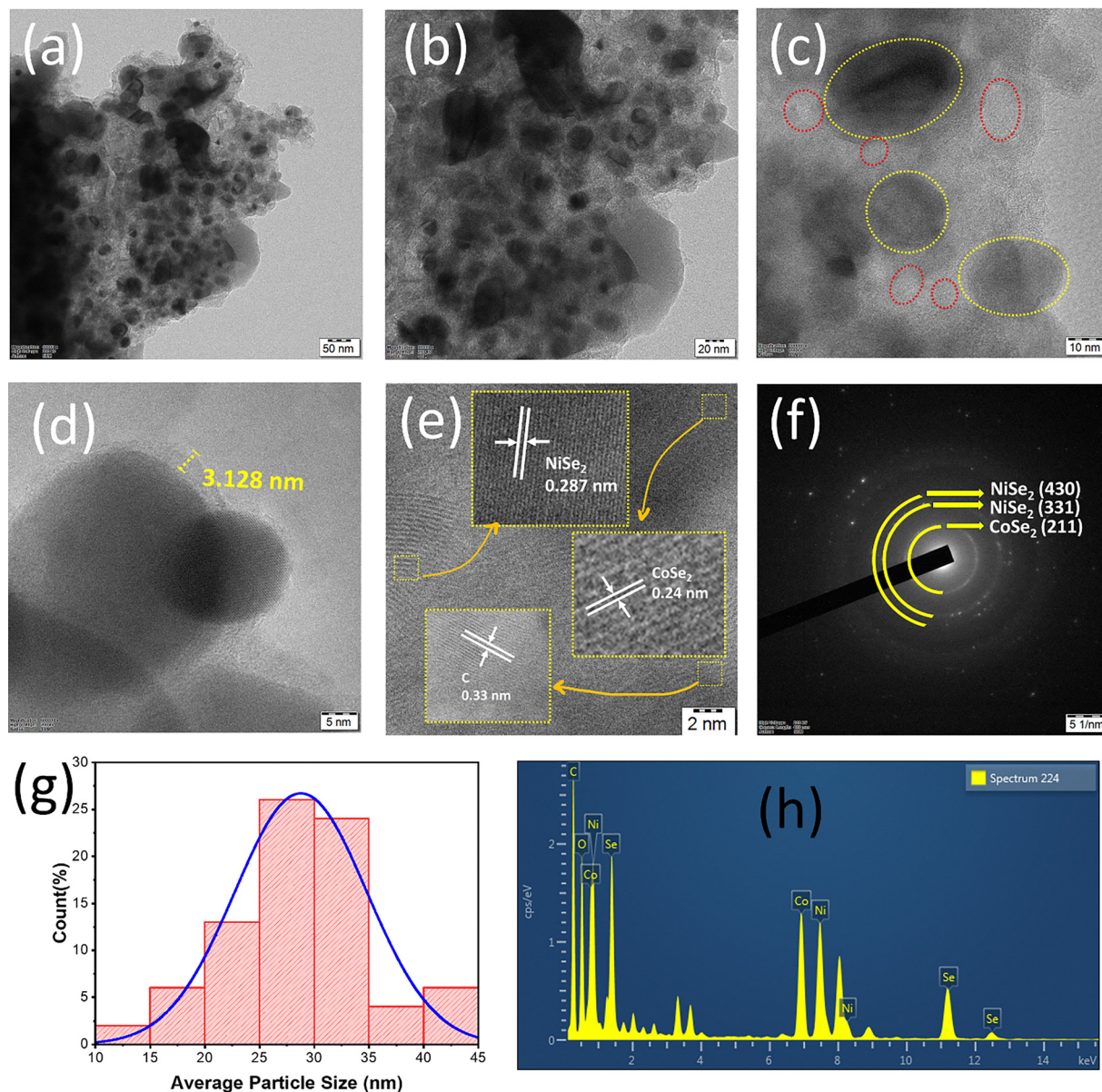
Fig. 4 TEM micrographs of GPC/NiSe$_2$/CoSe$_2$ showing a layer of conductive carbon along with spherical nickel and cobalt particles (a)–(e), corresponding SAED pattern (f), particle size distribution (g) and TEM-EDS (h).

The mesoporous structure generated post-carbonization can improve the mass transfer of reaction intermediates, hence facilitating the electrochemical catalysis of the material.[77,78] Subsequently, we attempted to ascertain how the substance interacts with water, the primary source for obtaining hydrogen. The contact angles of all three catalysts in water depicted in Fig. 5e and Fig. S10, and the results mentioned in Fig. 5f indicate that all samples exhibited contact angles lower than that of bare glass (C.A. = 50°). The minimal contact angle of the final composite, the GPC/NiSe$_2$/CoSe$_2$ sample, signifies superior hydrophilicity, and its hydrogen and oxygen production efficiency are excellent. This outcome aligns with the principle that enhanced hydrophilicity promotes advantageous chemical interactions. The surface of the sample treated by GPC/NiSe$_2$/CoSe$_2$ exhibited a greater adsorption of hydroxyl functional groups and demonstrated enhanced surface activity.[79]

3.4. Electrochemical HER activity

The electrocatalytic performance of the materials for the hydrogen evolution reaction was examined using LSV in a 0.1 M KOH solution at a scan rate of 25 mV s^{-1}. Fig. 6a–c represent the electrocatalytic HER data. The GPC/NiSe$_2$/CoSe$_2$ has superior catalytic activity, characterized by a markedly reduced η and an elevated J value compared to GPC, GPC/Ni, GPC/Co, and GPC/NiCo (Fig. 6a). The potential value at a current density of 10 mA cm^{-2} (η_{10}) is typically selected as the standard for HER catalysts, as solar-light-coupled HER systems generally function at 10–20 mA cm^{-2} under standard conditions (1 sun, AM 1.5).[80]
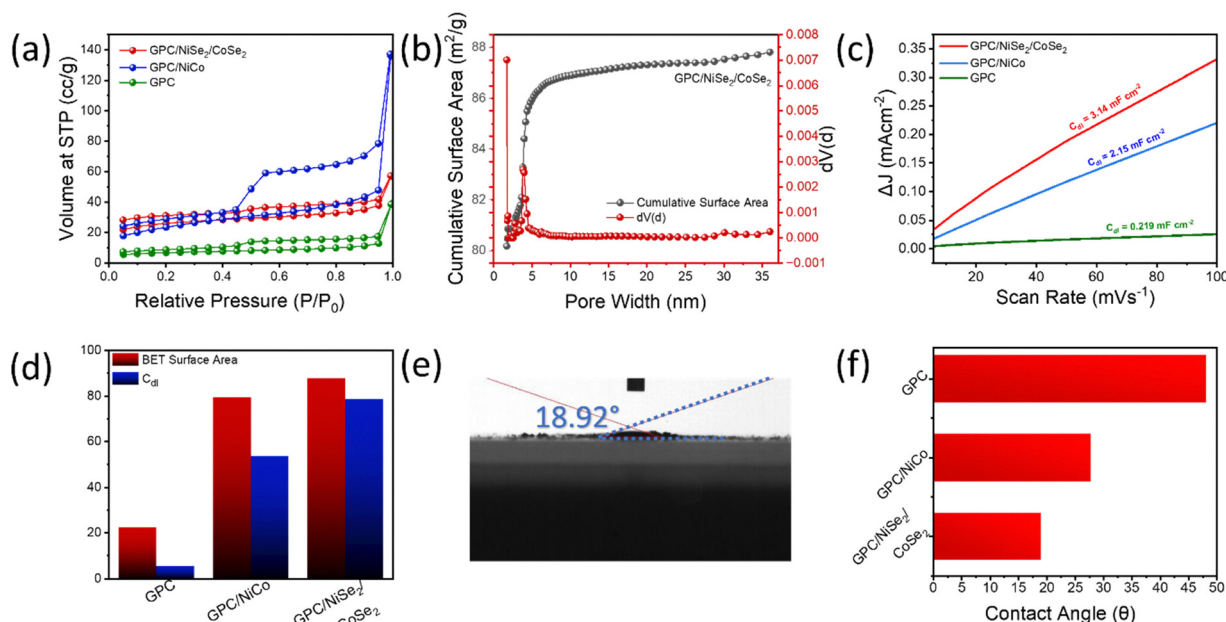
Fig. 5 (a) BET isotherms of GPC, GPC/NiCo and GPC/NiSe$_2$/CoSe$_2$. (b) Differential pore volume–pore width plot of GPC/NiSe$_2$/CoSe$_2$. (c) C_{dl} values of GPC, GPC/NiCo and GPC/NiSe$_2$/CoSe$_2$. (d) Comparison between BET Surface area and electrochemically active surface area for GPC, GPC/NiCo and GPC/NiSe$_2$/CoSe$_2$. (e) Contact angle measurement of GPC/NiSe$_2$/CoSe$_2$. (f) Bar diagram showing the contact angle of GPC, GPC/NiCo and GPC/NiSe$_2$/CoSe$_2$.

The improved GPC/NiSe$_2$/CoSe$_2$ necessitates an overpotential of merely 360 mV to provide a J value of 10 mA cm^{-2}. This is significantly better than that of the GPC (640 mV), GPC/Co (508 mV), GPC/Ni (495 mV), and GPC/NiCo (440 mV) (Fig. 6a). When comparing the HER activity across varying quantities of VN, specifically GPC/NiSe$_2$/CoSe$_2$ 45, 90, 135, and 180, GPC/NiSe$_2$/CoSe$_2$ 135 exhibits a markedly reduced η value compared to the others (Figure S12). Moreover, it exhibits the highest J value of 10 mA cm^{-2} at η of 360 mV among all synthesized samples, further indicating the exceptional performance of GPC/NiSe$_2$/CoSe$_2$ in the HER process. This can also be ascribed to the amplification of the synergistic action until the content of carbon reaches 135 mL. Exceeding this 135 mL limit, carbon atoms occupy the catalyst's active region, hence undermining the overall catalytic activity. As anticipated, commercial 20% Pt/C has the best electrocatalytic activity, characterized by a minimal onset overpotential of approximately 0 V. To gain additional understanding of the HER activity, and further elucidate the catalytic HER behavior regarding electron and mass transport as well as the reaction kinetics, the Tafel plots were fitted to the Tafel equation ($\eta = b\log(j) + a$, where η is the overpotential, b is the Tafel slope, and j signifies the current density) as depicted in Fig. 6b, based on linear sweep voltammetry measurements. The Tafel slope of Pt/C is 69.2 mV dec^{-1}, aligning with the reported value.[81] The Tafel slope of GPC/NiSe$_2$/CoSe$_2$ is 72.36 mV dec^{-1}, which is 165.75, 17.51, 55.69, and 6.19 mV dec^{-1} lower than those of GPC, GPC/Ni, GPC/Co, and GPC/NiCo, respectively. The Tafel slope of GPC/NiSe$_2$/CoSe$_2$ matches that of Pt/C (69.2 and 72.36 mV dec^{-1}). The comparison between all the catalysts is illustrated in Fig. 6c. The optimal mix of Ni, Co, Se and C, and the presence of pores

effectively modulates the electrical characteristics at the material surface, enhancing the activity and quantity of acceptor centers, which is more conducive to adsorption of H.[82] In an alkaline environment, the HER pathways include the adsorption of H$_2$O, and the electrochemical dissociation of H$_2$O into H$_{ads}$ and OH$^-$ species, followed by a desorption phase. The Tafel slope is an inherent property of the catalyst determined by the RDS (rate determining step) in the HER process. The calculation of the Tafel slope is crucial for elucidating the fundamental procedures involved. The observed Tafel slope of 69.2 mV dec^{-1} for Pt/C indicates that the hydrogen evolution reaction on the Pt surface proceeds through a Volmer–Tafel mechanism.[83] The Tafel slope of 72.36 mV dec^{-1} for the GPC/NiSe$_2$/CoSe$_2$ indicates that an effective hydrogen evolution reaction is facilitated through a Volmer–Heyrovsky mechanism, as evidenced by previous studies.[84] In this context, hydrogen production can be executed through two sequential reaction steps as outlined below:

$$\text{Volmer: } H_2O + e^- + * \rightarrow H* + OH^- \quad (1)$$

$$\text{Heyrovsky: } H* + H_2O + e^- \rightarrow H_2 + OH^- + * \quad (2)$$
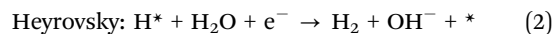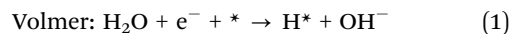
This mechanism is further supported by our Gibbs free-energy calculations and shows strong agreement with previously reported mechanistic studies on transition-metal and heteroatom-doped carbon catalysts, thereby reinforcing the validity of our findings.[85,86] Subsequently, electrochemical impedance spectroscopy (EIS) investigation was conducted to further understand the electrocatalytic activity of GPC/NiSe$_2$/CoSe$_2$ for the HER within a frequency range of 100 kHz to 0.05 Hz at open circuit potential (OCP). Figure S13 displays the
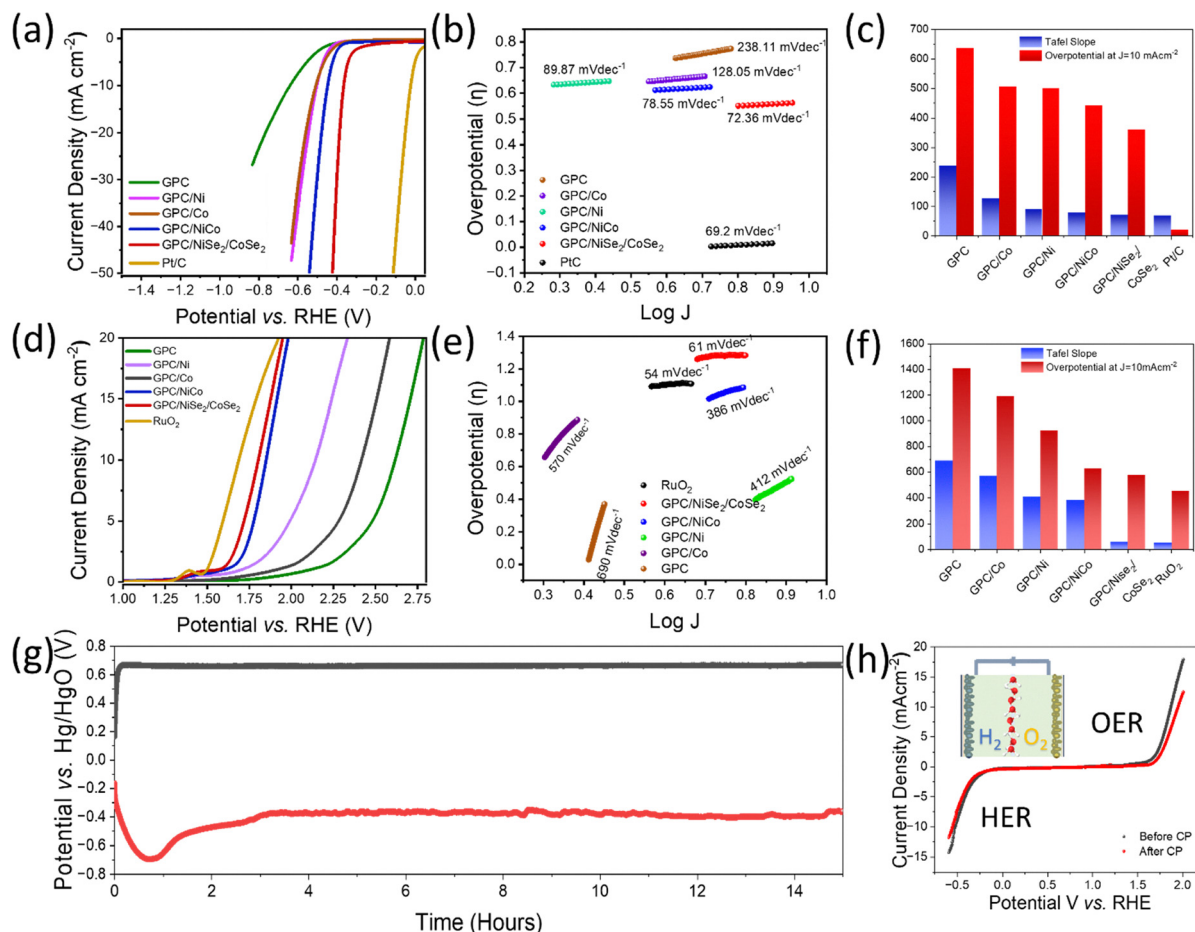
Fig. 6 Electrochemical water splitting (HER and OER) in 0.1M KOH solution. (a) and (d) Polarization LSV curves. (b) and (e) Corresponding Tafel plots and comparison of potential requirements at 10 mA cm^{-2} and Tafel slopes for all the catalysts (c) and (f). 16 hours long chronopotentiometry measurement (g) and the corresponding polarization curves before and after the measurement (h).

appropriate Nyquist plots. Among all materials, GPC/NiSe$_2$/CoSe$_2$ demonstrates the lowest charge transfer resistance value (R_{ct}) of merely 13.72 Ω, which is way less than GPC (81.37 Ω) and GPC/NiCo (17.78 Ω), and better ion diffusion efficiency compared to the others, correlating with its superior catalytic activities. The notable charge transfer kinetics and better catalytic activity may stem from the good synergistic interaction of nickel, cobalt, selenium, and nitrogen-doped carbon, thereby quenching the electrode resistance.

The stability of GPC/NiSe$_2$/CoSe$_2$ during the hydrogen evolution reaction was assessed *via* chronopotentiometry at a current density of 10 mA cm^{-2} (Fig. 6g and h). The increased firm wetting and activation of the inner zones and microporous regions of the electrode materials for ionic intercalation/de-intercalation during the long-term electrode stability experiments caused potential instability during the initial stages, and it showed no significant variation afterwards. For evaluating the catalyst's performance at larger current densities, chronopotentiometry was performed at a current density of 100 mA cm^{-2} (Fig. S20). As anticipated, the LSVs obtained before and after the stability experiment exhibited no variation in their overpotential values. The stability of GPC/NiSe$_2$/CoSe$_2$

was assessed again using LSV measurements by conducting 1000 cycles towards the HER (Fig. S14). In this context, the LSV results of the GPC/NiSe$_2$/CoSe$_2$ after a 1000 cycle procedure exhibited no significant variation in η and J compared to the first cycle, further indicating robust cycling stability during the HER. The outstanding HER performance of GPC/NiSe$_2$/CoSe$_2$ can be attributed to several factors based on the obtained data. Initially, a distinctive porous carbon skeletal structure enhances the electrocatalytic capabilities of the active material. Secondly, the efficient conversion of NiCo–Se to NiCo–OH enhances the active sites for adsorption.[87] Thirdly, metal selenides exhibit commendable conductivity for charge transfer but lack adequate active sites.[87] This issue is addressed here by employing a porous carbon skeleton, which offers a substantial surface area and mechanical stability. Consequently, the synthesis of bimetallic selenide nanoparticles on porous carbon can reduce electrical resistance while enhancing mechanical and catalytic stability.

3.5. Electrochemical OER activity

The electrochemical properties of the materials for the OER were assessed using LSV in 0.1 M KOH at a scan rate

of 25 mV s^{-1}. Fig. 6d illustrates the polarization curves for the GPC, GPC/Ni, GPC/Co, GPC/NiCo, GPC/NiSe$_2$/CoSe$_2$, and RuO$_2$ catalysts. All produced catalysts exhibit a pronounced anodic peak between 1.3 and 1.5 V, corresponding to the oxidation of Ni/Co species. Among the evaluated catalysts, the GPC/NiSe$_2$/CoSe$_2$ demonstrates an earlier onset potential, a lower η of 574 mV at J of 10 mA cm^{-2}, compared to GPC, GPC/Ni, GPC/Co, and GPC/NiCo, (Fig. 6d). The η value at 10 mA cm^{-2} for GPC/NiSe$_2$/CoSe$_2$ is 500 mV lower than that of GPC/NiCo, which turns out to be the second best. Addressing the current response to the OER, the J value of the GPC/NiSe$_2$/CoSe$_2$ at an overpotential of 500 mV is 57 mA cm^{-2}, significantly outperforming other produced materials. The electrocatalytic kinetics of the synthesized materials regarding the OER were examined using the associated Tafel plots (Fig. 6e). The Tafel slope of GPC/NiSe$_2$/CoSe$_2$ is 61 mV dec^{-1}, which is comparable to RuO$_2$ (54 mV dec^{-1}) and much lower than that of GPC (690 mV dec^{-1}), GPC/Co (570 mV dec^{-1}), GPC/Ni (412 mV dec^{-1}), and GPC/NiCo (366 mV dec^{-1}). The results indicate the formation of a carbon skeleton-supported bimetallic selenide morphology, wherein an optimal combination of Co–Ni–Se with a suitably doped nitrogen carbon ratio at the nanoscale enhances charge transfer and modulates the accessible surface-active sites. The selenide catalyst, supported on nitrogen-doped porous carbon, improves the conductivity and tendency for surface reconstruction, thus enhancing the formation of O–O bonds, therefore decreasing the activation energy required for the OER process.[72] The elevation in ECSA, seen by the C_{dl} readings in Fig. 5e, implies a greater number of exposed active sites of oxyhydroxides generated *in situ* during the OER.[88] These oxyhydroxides are considered essential constituents of nickel cobalt selenide that enhance OER performance.[89] Thus, in this case nitrogen-doped carbon is also co-doped with heteroatoms, cobalt and nickel selenides, which further augment the number of active sites, thus significantly enhancing catalytic activity. Consequently, the overall electrocatalytic activity of carbon for water splitting is enhanced by this synergistic coupling,[90] which also serves as a model for the study of its intrinsic electrocatalytic properties.

The durability of the GPC/NiSe$_2$/CoSe$_2$-based electrode for the oxygen evolution reaction was assessed using LSV following a comprehensive cycling procedure (Fig. S15). The acquired LSV demonstrate that the overpotential necessary to sustain a constant current density of 10 mA cm^{-2} exhibits no significant variation after 1000 cycles. The morphology of the electrocatalyst was analysed following the stability test, and the corresponding FESEM images are given in Fig. S5. The film's surface roughness was markedly enhanced following catalytic activity. The enhanced surface roughness is due to the release of evolved gas, which often forms a porous layer on the catalyst surface. Furthermore, prior studies indicate that the selenide catalyst maintains its composition even after rigorous stability assessments. Thus, this transition metal selenide electrocatalyst exhibited both functional durability and compositional stability following prolonged continuous gas evolution in an alkaline medium.[91] To elucidate the significant influence of the VN

extract-derived N-doped carbon support on the catalytic performance of the synthesized metal selenide, a NiSe$_2$/CoSe$_2$ sample was synthesized without the carbon support, using a chemical reducing agent, and the catalytic HER of NiSe$_2$/CoSe$_2$ was compared to that of GPC/NiSe$_2$/CoSe$_2$ under the same conditions. The GPC/NiSe$_2$/CoSe$_2$ demonstrates enhanced HER (Fig. S16) performance, evidenced by lower overpotential and improved current response compared to the NiSe$_2$/CoSe$_2$ material, highlighting the significant contribution of the carbon support VN in augmenting the efficacy of the GPC/NiSe$_2$/CoSe$_2$ skeleton for water splitting applications. The Tafel slopes and overpotential of the optimized catalyst were evaluated against previously reported catalysts, as seen in Fig. S17 and S18, indicating that GPC/NiSe$_2$/CoSe$_2$ ranks among the best earth-abundant catalysts presently available.

3.6. Overall water splitting

To evaluate the practical utility of GPC/NiSe$_2$/CoSe$_2$ for overall water splitting, GPC/NiSe$_2$/CoSe$_2$ based electrodes were employed as the anode and cathode in a water electrolysis system employing an H cell. In the H cell, the anode and cathode compartments were filled with 0.1M KOH separated by an anion exchange membrane.

Glassy carbon electrodes coated with GPC/NiSe$_2$/CoSe$_2$ were used as both electrodes (Fig. 7d). The overpotential for the HER and OER of the GPC/NiSe$_2$/CoSe$_2$(+)//GPC/NiSe$_2$/CoSe$_2$(−) in a 0.1 M KOH solution was measured as 0.496 V and 0.330 V, respectively (Fig. 7a), indicating the enhanced performance of our catalyst. Along with this, bubbles of hydrogen and oxygen were formed in the cathode and anode, respectively, shown in the inset of Fig. 7a. Also, the cyclic voltammetry plot (Fig. 7b) indicates a regenerative nature of the catalyst, which was further confirmed by chronopotentiometry analysis (Fig. 7c). The deviations in potential can be attributed to hydrogen generated at the surface of the electrode and then regained its potential once the bubble leaves the surface, at around 14 470 seconds. The potential first drops by 68% due to the initial stabilization for the first five hours and later only less than 12% is observed for the next 15 hours, proving the better stability of our material.

4. Theoretical study of GPC/NiSe$_2$/CoSe$_2$ towards electrochemical water splitting

To dive deeply into the underlying mechanisms of overall water splitting of the porous carbon supported transition metal selenide electrocatalysts, a computational study of the GPC supported electrocatalysts was done and the results were explored. In the detailed study, the supercells were arranged so that the unit cell vectors a and b lay within the surface plane, while the vector c was oriented perpendicular to this plane. Following optimization *via* DFT calculations, the lattice parameters of the catalyst were determined to be a = 7.41 Å and b = 7.42 Å, whereas the unit cell vector was fixed at c = 45.12 Å to
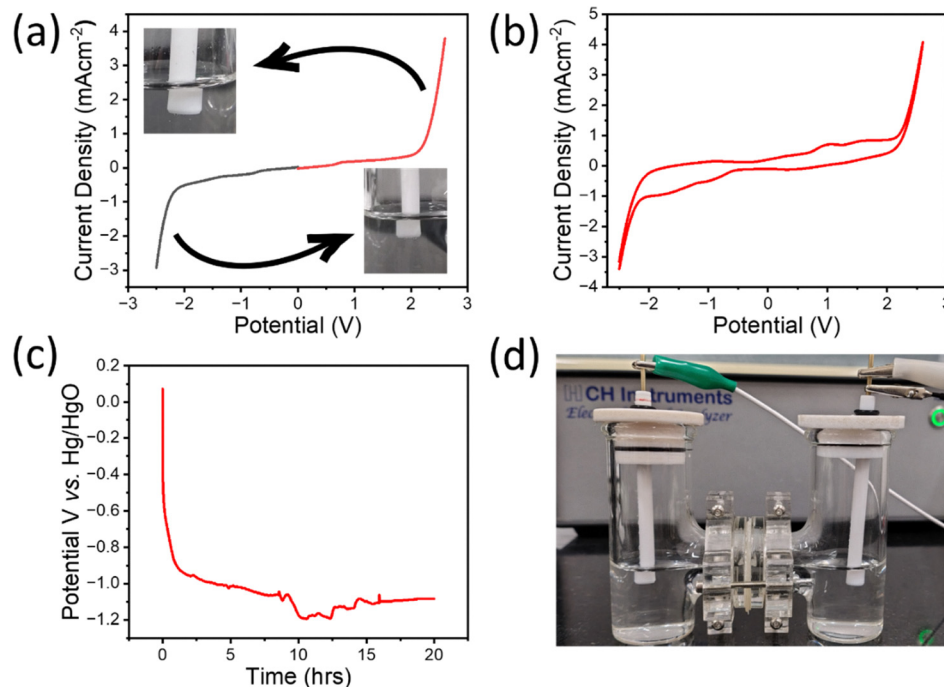
Fig. 7 (a) Polarisation curves of GPC/NiSe$_2$/CoSe$_2$//GPC/NiSe$_2$/CoSe$_2$ for overall water splitting. Bubbles of oxygen and hydrogen evolved in the inset. (b) Cyclic Voltammogram of the H cell setup indicating a regenerative nature of the catalyst. (c) 20 h chronopotentiometry test for overall water splitting performance of GPC/NiSe$_2$/CoSe$_2$. (d) Picture of the H cell setup with GCEs modified with GPC/NiSe$_2$/CoSe$_2$ employed as the anode and cathode. 0.1M KOH is used as an electrolyte and is filled in both compartments separated by an ion exchange membrane.

ensure sufficient separation and prevent interactions between periodic layers. The space group of the investigated heterocatalyst was identified as P1.

Analysis of hydrogen adsorption in the HER pathway revealed that hydrogen intermediates strongly bind to the Se atom of the catalyst, with a Se–H bond length of 1.50 Å. In the case of the OER, the bond distances between the intermediates and the catalyst varied between 1.84 Å and 1.98 Å. The hydroxyl (−OH) intermediate exhibited strong adsorption onto the selenium atom, forming a bond of 1.84 Å. Similarly, the hydroperoxyl (−OOH) intermediate displayed a strong binding interaction with selenium at a bond length of 1.92 Å. However, in the case of oxygen (−O) intermediate adsorption, oxygen formed a bridging structure between the Co and Se atom. The O–Co and O–Se bond distances were determined to be 1.98 Å and 1.76 Å, respectively. Fig. S11 provides a pictorial representation of the catalyst, depicting key intermediates involved in the HER and OER on the catalyst surface, along with important geometrical parameters.

The HER follows a three-state pathway, beginning with the initial state of H$^+$ + e$^-$, progressing through the adsorption of the H* intermediate, and ultimately leading to the formation of H$_2$ as the final product. The catalytic activity for the HER was assessed using the well-established descriptor ΔG_{H*}, where an optimal value of $|\Delta G_{H*}|$ should be close to zero to facilitate efficient hydrogen adsorption and desorption. As illustrated in Fig. 8(a), the calculated ΔG_{H*} value is 0.50 eV for H* adsorption onto the catalyst, indicating a strong adsorption strength of H*

intermediates. The near-zero ΔG_{H*} value indicates an optimal balance between hydrogen adsorption and desorption, implying theoretically favorable hydrogen evolution kinetics. Additionally, the measured hydrogen-metal (Se) bond distance of 1.50 Å suggests a low energy barrier and strong interaction between hydrogen and the Se atoms. This optimal ΔG_{H*} value, combined with the interaction with the Se atom, enhances HER kinetics and facilitates an efficient catalytic process, as demonstrated in Fig. 8a.

The oxygen evolution process was modelled using the conventional adsorbate evolution mechanism, which is widely recognized as the dominant pathway in this system.[92] Fig. 8b presents the geometrical configurations of the stable adsorbed intermediates. The transition metal atoms in the system exhibit significant electroactivity, playing a crucial role in stabilizing these intermediates and facilitating their transformation throughout the OER process. As depicted in Fig. 8b, the OER follows a four-electron transfer pathway, involving the sequential formation of OH, O, and OOH intermediates. The reaction initiates with the formation of OH intermediate onto the catalyst. This is followed by the sequential adsorption of O, OOH, and ultimately the evolution of O$_2$ gas.

At the standard potential ($U = 0$ V), the OER pathway exhibits a continuous uphill energy profile. The highest energy barrier occurs during the formation of [OH], with an energy value of 2.36 eV, identifying it as the rate-determining step (RDS). The calculated overpotential (1.13 V) provides a thermodynamic indicator of the intrinsic catalytic activity and helps elucidate
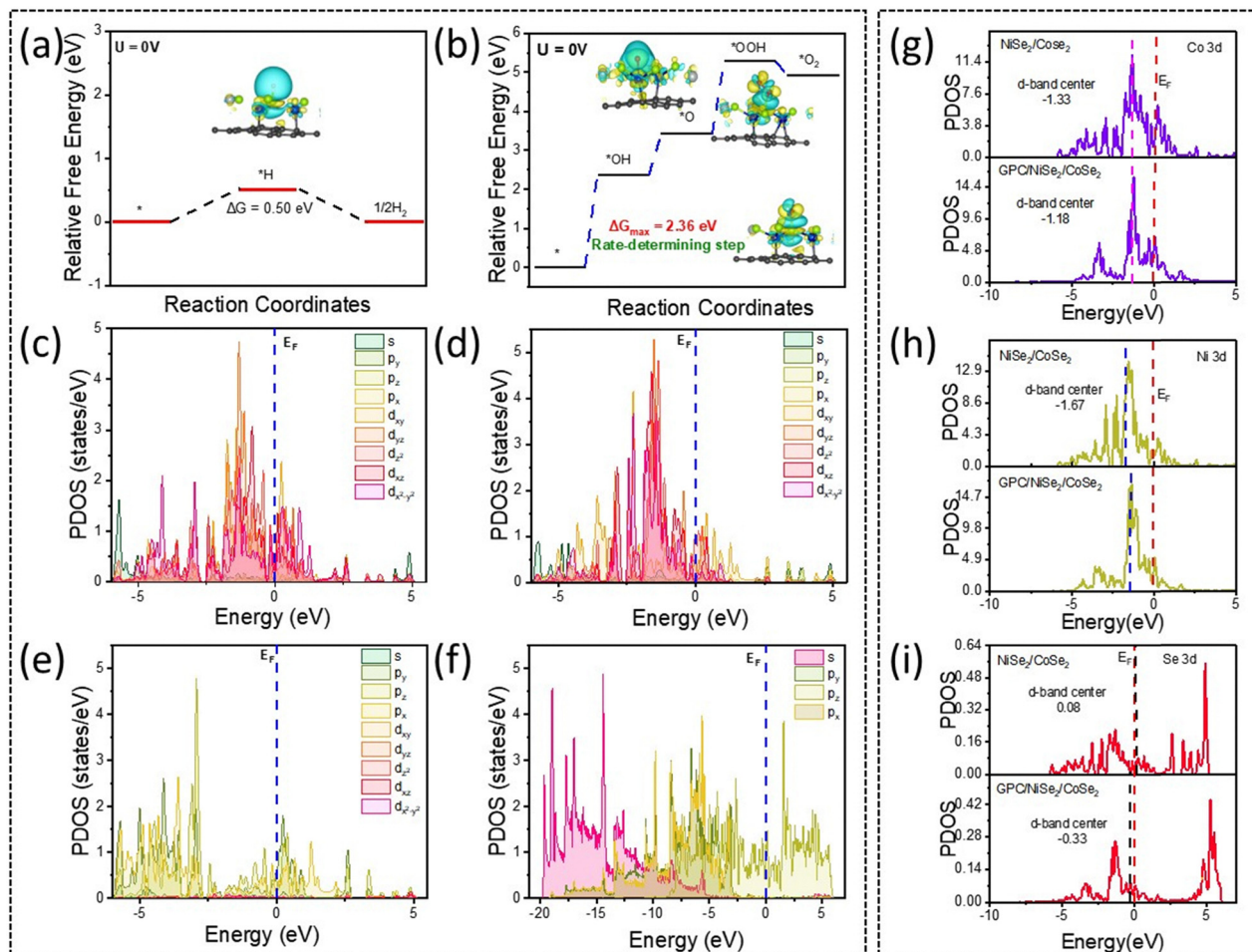
Fig. 8 Schematic representations are shown for (a) the free energy profile for the HER and (b) the free energy profile for the OER along with the differential charge density analysis at each intermediate step. The cyan color represents the charge depletion and the yellow color represents the charge accumulation. The Isosurface value used for the differential charge density analysis is 0.0013 a.u. Color code: Blue: Co, Green: Se, Grey: Ni, Dark Grey: C, PDOS of (c) Co, (d) Ni, (e) Se, and (f) C of GPC/NiSe$_2$/CoSe$_2$ catalyst. d-band center of (g) Co, (h) Ni, and (i) Se of the GPC/NiSe$_2$/CoSe$_2$ and NiSe$_2$/CoSe$_2$ catalyst.

the reaction energetics under idealized theoretical conditions (0 K, vacuum, and zero applied potential). This finding is in agreement with experimental analyses, confirming the catalytic influence on ORR activity. The structural evolution of the catalyst and the adsorbed species at each stage of the OER was further examined. Throughout the reaction, the intermediate species migrate from their initial position and bind to Se atoms located adjacent to Co and Ni on the catalyst surface. Notably, an increase in bond distance from the catalyst to the OH intermediate is observed, shifting from an initial Co–Se bond length of 2.28 Å to 2.32 Å after OH adsorption. The elongation of the Co–Se bond upon OH adsorption reflects surface relaxation and electronic redistribution associated with intermediate binding, indicative of significant electronic interaction between the adsorbate and the catalyst surface. However, a relatively smaller variation in bond distance occurs between successive intermediates, with a reduction of approximately 0.14 Å from OH to O and a further decrease of 0.04 Å in the transition to OOH. This systematic alteration in bond length

underscores the strong adsorption of OER intermediates onto the catalyst, which is essential for optimizing catalytic performance.

The charge distribution was further examined through differential charge density analysis, revealing significant modifications in the electronic structure of the heterocatalyst. The differential electron density plot demonstrated that the Se atom enhances electron density around the intermediates involved in both the HER and OER processes. Additionally, a notable variation in charge density was observed for Co and Ni atoms, indicating substantial electronic redistribution. The analysis further showed that the charge density differences exhibit a considerable disparity, suggesting an increased accumulation of electrons around the *H and *OH intermediates. This enhanced electron distribution plays a crucial role in improving HER and OER activity. The strong electronic coupling between Se, Co, and Ni facilitates a reduction in the reaction energy barrier and enhances electron transfer efficiency, thereby promoting catalytic performance.

Electronic property of GPC/NiSe$_2$/CoSe$_2$

To establish the intrinsic correlation between the electronic structure and catalytic activity in the HER and OER, an electronic property analysis was performed. Fig. 8(c–f) presents the calculated projected density of states (PDOS) of the catalyst, revealing a high concentration of electronic states near the Fermi level. This elevated electronic state density suggests enhanced electrical conductivity and improved electron transport during electrochemical reactions. For a more effective comparison, the PDOS was analyzed within the energy range of −5 to 5 eV.

As illustrated in Fig. 8(c–f), the catalyst exhibits metallic characteristics, as evidenced by the presence of electronic states at the Fermi level (E_F). The electron densities at E_F define the electroactive region, playing a crucial role in facilitating charge transfer. Additionally, a significant perturbation in the electronic distribution of the metal lattice is observed, leading to an electron-rich catalyst surface. This redistribution of electronic states further enhances catalytic performance by promoting efficient charge transport and reaction kinetics.

The PDOS analysis in Fig. 8 reveals that the metal-d states are primarily localized within the energy range of −5 to 3 eV, with metal sites contributing predominantly to the electronic states near the E_F. Additionally, the Se-p states exhibit electron-rich characteristics at lower energy levels. The metal-d orbitals demonstrate significant overlap with Se-p orbitals, facilitating efficient electron transfer between sites and promoting stable bonding interactions. Furthermore, the C-p states display notable electron distribution at E_F, indicating substantial electron transfer from carbon to the neighboring Se-metal sites, which enhances electroactivity. The strong orbital overlap between the p–p states of C and Se, as well as the p–d interactions among C, Se, and Co atoms, further supports significant electron delocalization. This tailored electronic structure results in an increased density of active electronic states at the catalytic sites, thereby significantly enhancing the overall catalytic performance.

Since OER kinetics is closely associated with the d-band center of transition metals,[93] the d-band of Co, Ni, and Se is presented in Fig. 8(g–i). The d-band center values were determined using a standard computational approach. For the GPC/NiSe$_2$/CoSe$_2$ system, the d-band centers of Co and Ni are calculated as −1.18 eV and −1.40 eV, respectively. In contrast, for the NiSe$_2$/CoSe$_2$ system, the d-band centers of Co and Ni are slightly shifted to −1.33 eV and −1.67 eV, respectively. This noticeable shift in the d-band center of Co and Ni in GPC/NiSe$_2$/CoSe$_2$ toward the Fermi level suggests an alteration in the electronic structure, influencing catalytic activity.

Additionally, the calculated d-band center for the Se atom in GPC/NiSe$_2$/CoSe$_2$ is found to be −0.33 eV. This shift toward the Fermi level indicates an enhancement in surface binding strength for reaction intermediates, which plays a crucial role in improving electrocatalytic performance. These findings align with the previously discussed mechanistic insights, further validating the role of electronic structure modifications in optimizing catalytic efficiency.[94,95]
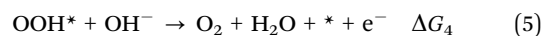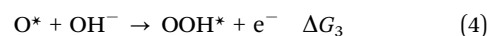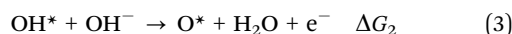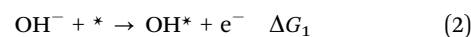
Reaction mechanism

The HER and OER pathways were analyzed using an electrochemical approach developed by Nørskov and colleagues.[92] Free-energy analysis was performed for the most active catalyst model to elucidate the structure–activity relationship and to gain theoretical insight into the intrinsic catalytic trends. The hydrogen adsorption free energy (ΔG_{H^*}) was determined using the relation:

$$\Delta G_{H^*} = \Delta E_{H^*} + \Delta ZPE - T\Delta S, \tag{1}$$

where ΔE_{H^*} represents the reaction energy change, ΔZPE corresponds to the zero-point energy correction, and ΔS denotes the entropy change.

In alkaline electrolytes, water molecules act as the primary source of protons, defining the complete reaction pathway for the OER as follows:

$$OH^- + * \rightarrow OH^* + e^- \quad \Delta G_1 \tag{2}$$

$$OH^* + OH^- \rightarrow O^* + H_2O + e^- \quad \Delta G_2 \tag{3}$$

$$O^* + OH^- \rightarrow OOH^* + e^- \quad \Delta G_3 \tag{4}$$

$$OOH^* + OH^- \rightarrow O_2 + H_2O + * + e^- \quad \Delta G_4 \tag{5}$$

Here, * represents an available catalytic adsorption site, while O, OH, and OOH denote the adsorbed reaction intermediates.

The Gibbs free energy (ΔG) for each elementary reaction step was calculated as:

$$\Delta G = \Delta E + \Delta ZPE - T\Delta S \tag{6}$$

where ΔE corresponds to the reaction energy derived from DFT computations, while ΔZPE and ΔS account for zero-point energy corrections and entropy changes, respectively. The Gibbs free energy values (ΔG_1, ΔG_2, ΔG_3, and ΔG_4) correspond to the reaction free energy for each step in eqn (2)–(5). Corrections for gas-phase molecular species were incorporated using reference data from the NIST database to ensure thermodynamic accuracy in the free energy calculations.

5. Conclusion

A simple and affordable method was designed for the synthesis of an adaptive catalyst comprising bimetallic Ni–Co Se particles supported on an optimum composition of nitrogen-doped hierarchically porous interconnected carbon framework. Also, the designed synthesis strategy was devoid of any chemical reducing agents, which most of the related systems will employ to reduce metal salts. Here, the extra load of reducing metal atoms was proceeded by the plant extract itself, in addition to acting as a carbon support, thanks to tons of phytochemicals present. The GPC/NiSe$_2$/CoSe$_2$ catalyst demonstrates superior catalytic activity for the hydrogen evolution reaction (0.36 V) and oxygen evolution reaction (0.57 V) compared to its oxide

and counterparts, as well as GPC, GPC/Ni, GPC/Co, GPC/NiCo and GPC/NiSe$_2$/CoSe$_2$ in an alkaline medium. The superior catalytic performance of transition metal selenides over their oxide counterparts arises from their distinctive electronic structure and strong metal–selenium covalent interactions. The involvement of Se 3d orbitals and cooperative bonding enhance electrical conductivity and facilitate charge transfer. These features collectively contribute to their rich redox activity and improved electrocatalytic efficiency. The HER and OER performance of the final optimized catalyst is comparable to that of commercial Pt/C and RuO$_2$. The exceptional performance of the GPC/NiSe$_2$/CoSe$_2$ catalyst may result from the synergistic interactions of Co, Ni, and Se, which are uniquely integrated to form distinctive nanoarchitectures on the surfaces of the nitrogen-doped porous carbon. This alters the electronic configuration of the catalyst and increases the available electroactive sites for controlling the adsorption energy of the reactants. Moreover, the extensive surface area and excellent conductivity play a crucial role by offering additional channels and reducing distances for rapid charge transfer, hence enhancing active surface exposure and mass diffusion pathways. The intrinsic association between electronic structure and catalytic activity in the HER and OER was established with the help of computational simulations and electronic property investigation. The PDOS of the catalyst indicated a higher concentration of electronic states closer to the Fermi level, which facilitates augmented electrical conductivity and boosted electron transport during electrochemical processes. This shift toward the Fermi level signifies an enhancement in surface binding strength for reaction intermediates, which is essential for boosting electrocatalytic efficiency. The outstanding performance of GPC/NiSe$_2$/CoSe$_2$ indicates its potential as a viable alternative for practical water-splitting applications. Ultimately, leveraging the benefits of facile preparation and earth abundance, transition metal selenides possess significant promise for industrial water splitting. Furthermore, we offer an economical and innovative combination of carbon support with a reducing agent derived from a single precursor, VN extract. This, in conjunction with increased activity, also compresses the reaction cascade.

Author contributions

The manuscript was written through the contributions of all authors. All authors have given approval to the final version of the manuscript.

Conflicts of interest

There are no conflicts to declare.

Data availability

Data files can be shared on reasonable request.

The data supporting this article have been included as part of the supplementary information (SI). Supplementary information is available. See DOI: https://doi.org/10.1039/d5ma00799b.

Acknowledgements

References

1 E. Panos, M. Densing and K. J. E. S. R. Volkart, *Energy Strategy Rev.*, 2016, **9**, 28–49.

2 J. Zhang, Z. Xia and L. Dai, *Sci. Adv.*, 2015, **1**, e1500564.

3 P. De Luna, C. Hahn, D. Higgins, S. A. Jaffer, T. F. Jaramillo and E. H. J. S. Sargent, *Science*, 2019, **364**, eaav3506.

4 N. S. Rathore and N. Panwar, *Renewable energy sources for sustainable development*, New India Publishing, 2007.

5 A. Demirbas, *Prog. Energy Combust. Sci.*, 2005, **31**, 171–192.

6 S. Sen and S. J. R. Ganguly, *Renewable Sustainable Energy Rev.*, 2017, **69**, 1170–1181.

7 M. W. Fazal, F. Zafar, M. Asad, F. M. H. Al Sulami, H. Khalid, A. A. Abdelwahab, M. U. Ur Rehman, N. Akhtar, W. A. El-Said and S. J. A. A. E. M. Hussain, *ACS Appl. Energy Mater.*, 2023, **6**, 2739–2746.

8 J. A. J. S. Turner, *Science*, 2004, **305**, 972–974.

9 Y. Zheng, Y. Jiao, M. Jaroniec and S. Z. J. A. C. I. E. Qiao, *Angew. Chem., Int. Ed.*, 2015, **54**, 52–65.

10 Z. W. Seh, J. Kibsgaard, C. F. Dickens, I. Chorkendorff, J. K. Nørskov and T. F. J. S. Jaramillo, *Science*, 2017, **355**, eaad4998.

11 H. Wang, S. Min, Q. Wang, D. Li, G. Casillas, C. Ma, Y. Li, Z. Liu, L.-J. Li and J. J. A. N. Yuan, *ACS Nano*, 2017, **11**, 4358–4364.

12 X. Zhao, X. Yong, Q. Ji, Z. Yang, Y. Song, Y. Sun, Z. Cai, J. Xu, L. Li and S. Shi, *J. Mater. Chem. A*, 2023, **11**, 12726–12734.

13 D. S. Su, S. Perathoner and G. J. Centi, *Chem. Rev.*, 2013, **113**, 5782–5816.

14 M. J. Allen, V. C. Tung and R. B. J. C. R. Kaner, *Chem. Rev.*, 2010, **110**, 132–145.

15 S. Zhou, L. Zhou, Y. Zhang, J. Sun, J. Wen and Y. Yuan, *J. Mater. Chem. A*, 2019, 7, 4217–4229.

16 H.-P. Feng, L. Tang, G.-M. Zeng, J. Tang, Y.-C. Deng, M. Yan, Y.-N. Liu, Y.-Y. Zhou, X.-Y. Ren and S. J. Chen, *J. Mater. Chem. A*, 2018, **6**, 7310–7337.

17 Y. Zhang, H. Pan, Q. Zhou, K. Liu, W. Ma and S. J. I. C. C. Fan, *Inorg. Chem. Commun.*, 2023, **153**, 110768.

18 B. Xing, F. Shi, Z. Jin, H. Zeng, X. Qu, G. Huang, C. Zhang, Y. Xu, Z. Chen and J. J. C. E. Lu, *Carbon Energy*, 2024, **6**, e633.

19 S. Ott, A. Orfanidi, H. Schmies, B. Anke, H. N. Nong, J. Hübner, U. Gernert, M. Gliech, M. Lerch and P. Strasser, *Nat. Mater.*, 2020, **19**, 77–85.

20 Y.-N. Wang, Z.-J. Yang, D.-H. Yang, L. Zhao, X.-R. Shi, G. Yang and B.-H. J. A. A. M. Han, *ACS Appl. Mater. Interfaces*, 2021, **13**, 8832–8843.

21 K. Lu, Z. Hu, J. Ma, H. Ma, L. Dai and J. J. N. C. Zhang, *Nat. Commun.*, 2017, **8**, 527.

22 Y. Luo, Y. Yan, S. Zheng, H. Xue and H. Pang, *J. Mater. Chem. A*, 2019, **7**, 901–924.

23 D. K. Sam, H. Li, Y.-T. Xu, Y. Cao and I. Science, *Adv. Colloid Interface Sci.*, 2024, 103279.

24 J. Song, C. Zhu, B. Z. Xu, S. Fu, M. H. Engelhard, R. Ye, D. Du, S. P. Beckman and Y. J. A. E. M. Lin, *Adv. Energy Mater.*, 2017, **7**, 1601555.

25 L. Yan, L. Cao, P. Dai, X. Gu, D. Liu, L. Li, Y. Wang and X. J. A. F. M. Zhao, *Adv. Funct. Mater.*, 2017, **27**, 1703455.

26 X. Xiao, C.-T. He, S. Zhao, J. Li, W. Lin, Z. Yuan, Q. Zhang, S. Wang, L. Dai and D. Yu, *Energy Environ. Sci.*, 2017, **10**, 893–899.

27 M. Kim, K. K. Leong, N. Amiralian, Y. Bando, T. Ahamad, S. M. Alshehri and Y. J. A. P. R. Yamauchi, *Appl. Phys. Rev.*, 2024, **11**, 041317.

28 S. De, A. M. Balu, J. C. van der Waals and R. J. C. Luque, *ChemCatChem*, 2015, **7**, 1608–1629.

29 Y. Ito, W. Cong, T. Fujita, Z. Tang and M. J. A. C. I. E. Chen, *Angew. Chem., Int. Ed.*, 2015, **54**, 2131–2136.

30 X. Zou, X. Huang, A. Goswami, R. Silva, B. R. Sathe, E. Mikmeková and T. J. A. C. Asefa, *Angew. Chem.*, 2014, **126**, 4461–4465.

31 X. Cui, P. Ren, D. Deng, J. Deng and X. J. E. Bao, *Energy Environ. Sci.*, 2016, **9**, 123–129.

32 M. Zang, N. Xu, G. Cao, Z. Chen, J. Cui, L. Gan, H. Dai, X. Yang and P. J. A. C. Wang, *ACS Catal.*, 2018, **8**, 5062–5069.

33 H. Jin, X. Wang, C. Tang, A. Vasileff, L. Li, A. Slattery and S. Z. J. A. M. Qiao, *Adv. Mater.*, 2021, **33**, 2007508.

34 X. Ding, D. Liu, P. Zhao, X. Chen, H. Wang, F. E. Oropeza, G. Gorni, M. Barawi, M. García-Tecedor and V. A. de la Peña O'Shea, *Nat. Commun.*, 2024, **15**, 5336.

35 Y. Sun, K. Xu, Z. Wei, H. Li, T. Zhang, X. Li, W. Cai, J. Ma, H. J. Fan and Y. J. A. M. Li, *Adv. Mater.*, 2018, **30**, 1802121.

36 H. Zhao, H. Zhang, G. Cui, Y. Dong, G. Wang, P. Jiang, X. Wu and N. J. A. C. B. E. Zhao, *Appl. Catal., B*, 2018, **225**, 284–290.

37 Y. Shi and B. J. C. S. R. Zhang, *Chem. Soc. Rev.*, 2016, **45**, 1529–1541.

38 W. Feng, W. Pang, Y. Xu, A. Guo, X. Gao, X. Qiu and W. J. C. Chen, *ChemElectroChem*, 2020, **7**, 31–54.

39 K. L. Zhou, Z. Wang, C. B. Han, X. Ke, C. Wang, Y. Jin, Q. Zhang, J. Liu, H. Wang and H. J. N. C. Yan, *Nat. Commun.*, 2021, **12**, 3783.

40 R. Sun, Z.-H. Su, Z.-F. Zhao, M.-Q. Yang, T.-S. Li, J.-X. Zhao and Y.-C. Shang, *Rare Met.*, 2023, **42**, 3420–3429.

41 H.-B. Wang, Y.-S. Sun, F. Ma, L. Zhou, H.-F. Li, L. Zhang, G.-J. Chen, Y.-K. Xu, Y.-N. Chen and K.-W. J. Xu, *J. Alloys Compd.*, 2020, **819**, 153056.

42 A. Sobhani and M. J. A. i C. Salavati-Niasari, *Adv. Colloid Interface Sci.*, 2021, **287**, 102321.

43 X. Peng, Y. Yan, X. Jin, C. Huang, W. Jin, B. Gao and P. K. J. N. E. Chu, *Nano Energy*, 2020, **78**, 105234.

44 Y. Wang, L. Liu, Y. Wang, L. Fang, F. Wan and H. J. N. Zhang, *Nanoscale*, 2019, **11**, 6108–6119.

45 X. Xu, H. Liang, F. Ming, Z. Qi, Y. Xie and Z. J. A. C. Wang, *ACS Catal.*, 2017, **7**, 6394–6399.

46 T. Wang, H. C. Chen, F. Yu, X. Zhao and H. J. E. S. M. Wang, *Energy Storage Mater.*, 2019, **16**, 545–573.

47 C. J. Zheng, H. Q. Li, S. C. Ren, C. L. Xu, K. Rahman, L. P. Qin and Y. H. J. P. R. Sun, *Phytother. Res.*, 2015, **29**, 633–647.

48 P. Zhou, F. Xiao, R. Weng, Q. Huang, L. Wang, Q. He, W. Tang, P. Yang, R. Su and P. He, *J. Mater. Chem. A*, 2022, **10**, 10514–10524.

49 N. Deng, W. Kang, J. Ju, L. Fan, X. Zhuang, X. Ma, H. He, Y. Zhao and B. Cheng, *J. Power Sources*, 2017, **346**, 1–12.

50 M. Sevilla, R. Mokaya and A. B. Fuertes, *Energy Environ. Sci.*, 2011, **4**, 2930–2936.

51 S. Karingula, S. Kummari, Y. G. Kotagiri, T. Bhookya and K. V. J. S. Gobi, *Small*, 2024, 2400812.

52 G. Kresse and J. J. P. r B. Furthmüller, *Phys. Rev. B:Condens. Matter Mater. Phys.*, 1996, **54**, 11169.

53 J. P. Perdew, K. Burke and M. Ernzerhof, *Phys. Rev. Lett.*, 1996, **77**, 3865.

54 P. E. Blöchl, *Phys. Rev. B:Condens. Matter Mater. Phys.*, 1994, **50**, 17953.

55 L. S. Pedroza, A. J. da Silva, K. J. P. R. B. C. M. Capelle and M. Physics, *Phys. Rev. B:Condens. Matter Mater. Phys.*, 2009, **79**, 201106.

56 J. P. Perdew, A. Ruzsinszky, G. I. Csonka, O. A. Vydrov, G. E. Scuseria, L. A. Constantin, X. Zhou and K. Burke, *Phys. Rev. Lett.*, 2008, **100**, 136406.

57 G. Kresse and J. Furthmüller, *Comput. Mater. Sci.*, 1996, **6**, 15–50.

58 H. J. Monkhorst and J. D. J. P. r B. Pack, *Phys. Rev. B*, 1976, **13**, 5188.

59 S. Karingula, S. K. Venishetty, Y. G. Kotagiri and K. V. Gobi, *J. Energy Storage*, 2024, **75**, 109641.

60 I. Shaheen, K. S. Ahmad, C. Zequine, R. K. Gupta, A. G. Thomas and M. A. Malik, *Energy*, 2021, **218**, 119502.

61 R. Takahashi, S. Sato, T. Sodesawa and Y. Kamomae, *Phys. Chem. Chem. Phys.*, 2000, **2**, 1199–1204.

62 Z. Rahmati, M. Roushani, H. J. S. Hosseini and A. B. Chemical, *Sens. Actuators, B*, 2020, **324**, 128730.

63 M. Sangeetha Vidhya, R. Yuvakkumar, G. Ravi, A. G. Al-Sehemi, V.-H. Nguyen and D. Velauthapillai, *Energy Fuels*, 2022, **36**, 1726–1734.

64 V. Murugadoss, P. Panneerselvam, C. Yan, Z. Guo and S. J. E. A. Angaiah, *Electrochim. Acta*, 2019, **312**, 157–167.

65 J. Zhang, Q. Zhang, X. Qu, G. Xu, B. Fan, Z. Yan, F. Gui and L. J. A. S. S. Yang, *Appl. Surf. Sci.*, 2022, **574**, 151559.

66 L. Xie, W. Zhang, X. Chen, R. Shan, Q. Han, X. Qiu, N. Oli, J. F. Florez Gomez, L. Zhu and X. Wu, *ACS Appl. Mater. Interfaces*, 2023, **15**, 25536–25549.

67 S. Song, F. Ma, G. Wu, D. Ma, W. Geng and J. Wan, *J. Mater. Chem. A*, 2015, **3**, 18154–18162.

68 Y. Liu, H. Jiang, Y. Zhu, X. Yang and C. Li, *J. Mater. Chem. A*, 2016, **4**, 1694–1701.

69 B. Li, F. Dai, Q. Xiao, L. Yang, J. Shen, C. Zhang and M. Cai, *Energy Environ. Sci.*, 2016, **9**, 102–106.

70 Q. Xiao, Q. Song, K. Zheng, L. Zheng, Y. Zhu and Z. J. N. E. Chen, *Nano Energy*, 2022, **98**, 107326.

71 S. Chen, H. Ma, X. Zhou, D. Jin, J. Yan, G. Wang, W. Zhao, J. Yun, H. Zhang and Z. Zhang, *ACS Appl. Energy Mater.*, 2022, **6**, 424–438.

72 S. Anantharaj and S. Noda, *Int. J. Hydrogen Energy*, 2020, **45**, 15763–15784.

73 V. López, R. S. Sundaram, C. Gómez-Navarro, D. Olea, M. Burghard, J. Gómez-Herrero, F. Zamora and K. J. A. M. Kern, *Adv. Mater.*, 2009, **21**, 4683–4686.

74 Z.-Y. Yu, Y. Duan, M.-R. Gao, C.-C. Lang, Y.-R. Zheng and S.-H. Yu, *Chem. Sci.*, 2017, **8**, 968–973.

75 C. Dong, X. Yuan, X. Wang, X. Liu, W. Dong, R. Wang, Y. Duan and F. Huang, *J. Mater. Chem. A*, 2016, **4**, 11292–11298.

76 F. Guo, Z. Liu, Y. Zhang, J. Xiao, X. Zeng, C. Zhang, P. Dong, T. Liu, Y. Zhang and M. Li, *ACS Appl. Mater. Interfaces*, 2022, **14**, 24447–24461.

77 L. Wang, Z. Tang, W. Yan, Q. Wang, H. Yang and S. Chen, *J. Power Sources*, 2017, **343**, 458–466.

78 K. Shen, W. Qian, N. Wang, C. Su and F. Wei, *J. Am. Chem. Soc.*, 2013, **135**, 15322–15325.

79 K. Li, L. Bao, S. Cao, Y. Xue, S. Yan and H. Gao, *ACS Appl. Energy Mater.*, 2021, **4**, 12965–12973.

80 J.-S. Li, Y. Wang, C.-H. Liu, S.-L. Li, Y.-G. Wang, L.-Z. Dong, Z.-H. Dai, Y.-F. Li and Y.-Q. Lan, *Nat. Commun.*, 2016, **7**, 11204.

81 X. Chen, G. Liu, W. Zheng, W. Feng, W. Cao, W. Hu and P. Hu, *Adv. Funct. Mater.*, 2016, **26**, 8537–8544.

82 G. J. J. C. r Kubas, *Chem. Rev.*, 2007, **107**, 4152–4205.

83 Y. Zhang, Q. Shao, S. Long and X. J. N. E. Huang, *Nano Energy*, 2018, **45**, 448–455.

84 N. Mahmood, Y. Yao, J. W. Zhang, L. Pan, X. Zhang and J. J. J. A. S. Zou, *Adv. Sci.*, 2018, **5**, 1700464.

85 Y. Jiao, Y. Zheng, K. Davey and S.-Z. Qiao, *Nat. Energy*, 2016, **1**, 1–9.

86 L. Bai, C.-S. Hsu, D. T. Alexander, H. M. Chen and X. Hu, *Nat. Energy*, 2021, **6**, 1054–1066.

87 X. Xia, L. Wang, N. Sui, V. L. Colvin and W. Y. J. N. William, *Nanoscale*, 2020, **12**, 12249–12262.

88 G. Li, L. Anderson, Y. Chen, M. Pan and P.-Y. A. Chuang, *Sustainable Energy Fuels*, 2018, **2**, 237–251.

89 Z. J. E. T. Wu, *Energy Technol.*, 2024, **12**, 2301574.

90 X. Guanghui, X. Qingfeng, H. Qin, Y. Meitong, G. Bingshou, D. Rui, W. Yao, Y. Yigang, C. Yungui and W. J. C. E. J. Chaoling, *Chem. Eng. J.*, 2024, 153405.

91 X. Cao, Y. Hong, N. Zhang, Q. Chen, J. Masud, M. A. Zaeem and M. Nath, *ACS Catal.*, 2018, **8**, 8273–8289.

92 J. K. Nørskov, J. Rossmeisl, A. Logadottir, L. Lindqvist, J. R. Kitchin, T. Bligaard and H. Jonsson, *J. Phys. Chem. B*, 2004, **108**, 17886–17892.

93 W. Li, J. Liu, P. Guo, H. Li, B. Fei, Y. Guo, H. Pan, D. Sun, F. Fang and R. Wu, *Adv. Energy Mater.*, 2021, **11**, 2102134.

94 H. Wu, Q. Zhai, F. Ding, D. Sun, Y. Ma, Y. Ren, B. Wang, F. Li, H. Bian and Y. Yang, *Dalton Trans.*, 2022, **51**, 14306–14316.

95 S. Ni, H. Qu, Z. Xu, X. Zhu, H. Xing, L. Wang, J. Yu, H. Liu, C. Chen and L. Yang, *Appl. Catal., B*, 2021, **299**, 120638.